INTERNATIONAL JOURNAL FOR NUMERICAL METHODS IN FLUIDS
*Int. J. Numer. Meth. Fluids* 2009; **59**:559–575
Published online 2 June 2008 in Wiley InterScience (www.interscience.wiley.com). DOI: 10.1002/fld.1834

# Healing of shock instability for Roe's flux-difference splitting scheme on triangular meshes

Sutthisak Phongthanapanich[1] and Pramote Dechaumphai[2,*,†]

[1]*Department of Mechanical Engineering Technology, College of Industrial Technology, King Mongkut's University of Technology North Bangkok, Bangkok 10800, Thailand*
[2]*Department of Mechanical Engineering, Chulalongkorn University, Bangkok 10330, Thailand*

SUMMARY

Healing of nonphysical flow solutions and shock instability from the use of Roe's flux-difference splitting scheme is presented. The proposed method heals nonphysical flow solutions such as the carbuncle phenomenon, the shock instability from the odd–even decoupling problem, and the expansion shock generated from the violated entropy condition. The performance and efficiency of the proposed method are evaluated by solving several benchmark and complex high-speed compressible flow problems. Copyright © 2008 John Wiley & Sons, Ltd.

Received 8 May 2007; Revised 27 March 2008; Accepted 1 April 2008

KEY WORDS: carbuncle phenomenon; shock instability; $H$-correction entropy fix; Roe's FDS

## 1. INTRODUCTION

During the past decades, a variety of shock-capturing schemes have been developed for solving the Euler equations of gas dynamics. The Godunov method has been widely used and shown to produce high precision for simulations of complex shock phenomena. However, the method has some weakness and may fail or produce physically unrealistic numerical solutions for some problems. These problems include the high Mach number flow past a blunt body [1] and the moving shock in a straight duct from an odd–even grid perturbation [2].

Similar to the Godunov method, the original Roe's scheme has been widely employed and applied to solve complex flow problems. The scheme was also found to produce physically unrealistic expansion shock for flow over a forward-facing step because it does not satisfy the entropy condition

*Correspondence to: Pramote Dechaumphai, Department of Mechanical Engineering, Chulalongkorn University, Bangkok 10330, Thailand.
†E-mail: fmepdc@eng.chula.ac.th

Contract/grant sponsor: Thailand Research Fund

[3]. Some numerical experiments have shown that the extension of the one-dimensional upwind scheme to multidimensional problems often yields poor stationary shock at high Mach number aligned with the structured mesh. To overcome this problem, Harten [3] and Van Leer *et al.* [4] proposed the entropy fix formulation to replace the near-zero eigenvalues by some tolerances.

Lately, Sanders *et al.* [5] showed that the crossflow dissipation from such an upwind scheme may be inadequate due to the failure of grid alignment. These authors then proposed a multidimensional method, called the $H$-correction method. This method consists in introducing the largest one-dimensional correction from all the neighboring cell interfaces. Pandolfi and D'Ambrosio [6] later suggested a modified version of the $H$-correction method by excluding the one-dimensional correction of the cell interface between the left and right cells from the characteristic speed difference evaluation and then applied it to the vorticity and entropy waves only.

The main objective of this paper is to propose a mixed multidimensional entropy fix method and compare its numerical solutions with those obtained from the existing entropy fix methods for a two-dimensional high-speed compressible flow analysis on a structured triangular mesh. The entropy fix methods [4, 6] are modified herein for an unstructured triangular mesh and implemented into the original Roe's scheme.

Section 2 describes some well-known problems that exhibit the numerical shock instability from Roe's scheme. The existing entropy fix methods [4–6] and the proposed mixed multidimensional entropy fix method are examined to evaluate their solution accuracy. Finally, the proposed method is further extended to achieve higher-order solution accuracy and then evaluated by several benchmark test cases in Section 3 for solving both steady-state and transient high-speed compressible flow problems.

## 2. SOME FAILURE OF ROE'S SCHEME AND ITS HEALING

Some of the problems presented in this section are chosen to illustrate the failure of Roe's scheme to yield correct solutions to the compressible Euler equations. Physical unrealistic numerical solutions may arise from the implementation of the one-dimensional upwinding numerical flux function into the multidimensional formulation. To avoid such solutions, three entropy fix methods [4–6] have been recently proposed because of their simplicity and convenience for code implementation. A mixed multidimensional entropy fix method is proposed in this paper. The details of these entropy fix methods are presented herein and their performance is assessed for several test cases. All solutions in this section are obtained by using Roe's scheme with the first-order accuracy on a structured triangular mesh.

### 2.1. Roe's flux-difference splitting scheme and entropy fix

The Euler equations for a two-dimensional inviscid flow are given as

$$\frac{\partial}{\partial t}\int_{\Omega}\mathbf{U}\,\mathrm{d}\Omega+\int_{\partial\Omega}\mathbf{F}\cdot\hat{\mathbf{n}}\,\mathrm{d}S=0 \tag{1}$$

where $\mathbf{U}$ is the vector of conservative variables, $\mathbf{F}$ is the numerical flux vector and $\hat{\mathbf{n}}$ is the normal unit vector to the cell boundary. The equation of state of a perfect gas is in the following form:

$$p=\rho e(\gamma-1) \tag{2}$$



DOI: 10.1002/fld

where $p$ is the pressure, $\rho$ is the density, $e$ is the internal energy, and $\gamma$ is the specific heat ratio. The numerical flux vector at the cell interface between the left cell $L$ and the right cell $R$ according to Roe's scheme [7] is expressed as

$$\mathbf{F}_n = \frac{1}{2}(\mathbf{F}_{nL} + \mathbf{F}_{nR}) - \frac{1}{2}\sum_{k=1}^{4} \alpha_k |\lambda_k| \mathbf{r}_k \tag{3}$$

where $\lambda_k = \lfloor V_n - a \;\; V_n \;\; V_n \;\; V_n + a \rfloor^{\mathrm{T}}$, $\alpha_k$ is the wave strength of the $k$th wave, $\mathbf{r}_k$ is the corresponding right eigenvector, $V_n$ is the normal velocity, and $a$ is the speed of sound at the cell interface.

The original Roe's scheme ($\mathscr{Roe}$) was found to produce nonphysical solutions for the Euler equations in certain problems such as the expansion shock that violates the entropy condition. Many entropy fix methods were then proposed and investigated. These include Van Leer's entropy fix method ($\mathscr{RoeVL}$) where the characteristic speeds of the acoustic waves (for $k=1$ and 4) are replaced by the one-dimensional entropy fix as follows:

$$|\lambda_k|^* = \begin{cases} |\lambda_k|, & |\lambda_k| \geqslant 2\eta^{\mathrm{VL}} \\ \dfrac{|\lambda_k|^2}{4\eta^{\mathrm{VL}}} + \eta^{\mathrm{VL}}, & |\lambda_k| < 2\eta^{\mathrm{VL}} \end{cases} \tag{4}$$

where $\eta^{\mathrm{VL}} = \max(\lambda_R - \lambda_L, 0)$.

Sanders *et al.* [5] introduced an idea of a multidimensional dissipation, or the so-called $H$-correction entropy fix method as shown in Figure 1(a). The advantages of the method are the simplicity of its implementation into the existing scheme and the parameter-free characteristics. For two triangular cells shown in Figure 1(b), the corresponding $H$-correction entropy fix ($\mathscr{RoeSA}$) has been modified by Dechaumphai and Phongthanapanich [8]:

$$\eta^{\mathrm{SA}} = \max(\eta_1, \eta_2, \eta_3, \eta_4, \eta_5) \tag{5}$$

where $\eta_i = 0.5 \max_k(|\lambda_{i,kR} - \lambda_{i,kL}|)$.

Pandolfi and D'Ambrosio [6] proposed another version of the $H$-correction entropy fix ($\mathscr{RoePA}$) on a structured mesh. The method excludes $\eta_1$ from Equation (5) to avoid an erroneous injection of artificial viscosity and is applicable only to the entropy and vorticity waves (for $k=2$ and 3):

$$\eta^{\mathrm{PA}} = \max(\eta_2, \eta_3, \eta_4, \eta_5) \tag{6}$$

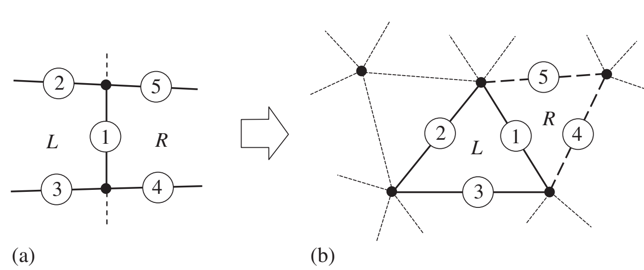


Figure 1. Cell interfaces: (a) structured uniform mesh and (b) unstructured triangular mesh.



DOI: 10.1002/fld

The method was used to study the shock wave reflection in a steady supersonic flow [9]. It has been found that the above three methods, namely the $\mathscr{RoeVL}$, $\mathscr{RoeSA}$, and $\mathscr{RoePA}$, perform well in some problems but may fail in others. For example, as will be presented later, the $\mathscr{RoeVL}$ can perform very well for flow with the expansion shock that contains the sonic point, such as flow over a forward-facing step. The $\mathscr{RoePA}$ is suitable for eliminating the numerical instability from the insufficient dissipation injected to the entropy and vorticity waves, such as the kinked Mach stem problem and flow over a blunt body. This paper thus proposes a mixed multidimensional entropy fix method ($\mathscr{RoeVLPA}$) that combines the entropy fix methods of Van Leer *et al.* [4] and Pandolfi and D'Ambrosio [6] by modifying the original eigenvalues as follows:

$$|\lambda_k| = \begin{cases} |\lambda_{1,4}|, & |\lambda_{1,4}| \geqslant 2\eta^{\mathrm{VL}} \\ \dfrac{|\lambda_{1,4}|^2}{4\eta^{\mathrm{VL}}} + \eta^{\mathrm{VL}}, & |\lambda_{1,4}| < 2\eta^{\mathrm{VL}} \\ \kappa \max(|\lambda_{2,3}|, \eta^{\mathrm{PA}}) \end{cases} \tag{7}$$

The constant value $\kappa$ is usually less than or equal to 1 for a first-order scheme and more than 1 for a higher-order scheme. After performing the numerical experiment, the value of $\kappa$ is problem-dependent in the case of the higher-order scheme. An appropriate range of $\kappa$ for the higher-order scheme is between 1.5 and 6.5, with the recommended value of 2. The sensitivity of the value of $\kappa$ to the density and pressure perturbations for the odd–even decoupling problem is investigated as shown in Figures 8 and 9 and is explained in more detail at the end of this section. The figures show that higher values of $\kappa$ yield more damping rate for the density and pressure perturbations. Thus, for simplicity, the value of $\kappa$ is taken to be 1 throughout this paper, or otherwise a certain value is specified when appropriate. This proposed entropy fix method ($\mathscr{RoeVLPA}$) is equivalent to the $\mathscr{RoeVL}$ to handle the acoustic waves and the $\mathscr{RoePA}$ for the entropy and vorticity waves.

In the following sections, the above four methods have been evaluated using four test cases. These include the carbuncle phenomenon, the odd–even decoupling, the kinked Mach stem, and the expansion shock. These test cases highlight the performance of the $\mathscr{RoePA}$, $\mathscr{RoeSA}$, $\mathscr{RoeVL}$, and the proposed $\mathscr{RoeVLPA}$ compared with the $\mathscr{Roe}$ in problems of different flow phenomena using the structured triangular mesh.

### 2.2. *The carbuncle phenomenon*

The carbuncle phenomenon is often referred to as a spurious bump on the bow shock near the flow centerline ahead the blunt body [1]. The problem is represented as a Mach 15 inviscid flow over a circular cylinder. The uniform upstream values are imposed on the left boundary while the slip wall boundary is prescribed along the circular surface, and the outflow conditions are given along the other boundaries. The phenomenon is highly grid-dependent but does not require a large number of grid points [6, 10]. To demonstrate the grid-dependent results, all the methods are employed with meshes of three different element aspect ratios. The numerical solutions shown in Figures 2–4 are the snapshots of the results obtained after performing 12 000 iterations. Figures 2–4 show three meshes with the same number of 15 nodes in the radial direction, but with a different number of nodes (60, 140, and 280, respectively) in the circumferential direction. The density contours of the first mesh ($15\times 60$ nodes) are shown in Figure 2(a)–(e). The carbuncle phenomenon does not appear in any scheme with this relatively crude mesh. The second mesh ($15\times 140$ nodes) has more

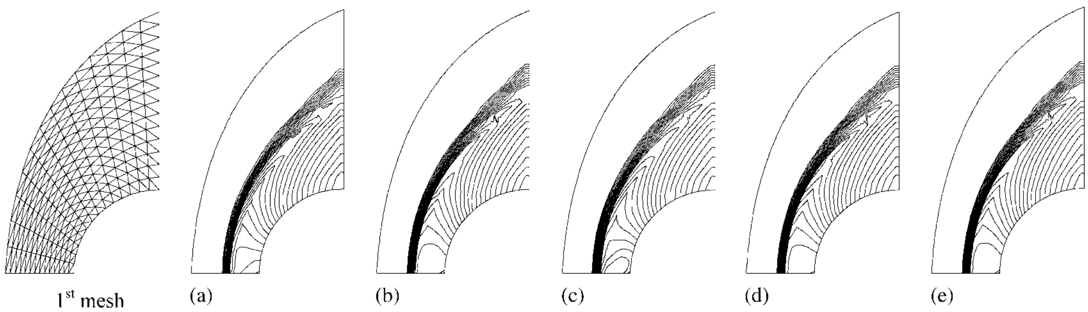


Figure 2. Density contours of a Mach 15 flow over a blunt body (first mesh): (a) $\mathscr{Roe}$; (b) $\mathscr{RoePA}$; (c) $\mathscr{RoeSA}$; (d) $\mathscr{RoeVL}$; and (e) $\mathscr{RoeVLPA}$.

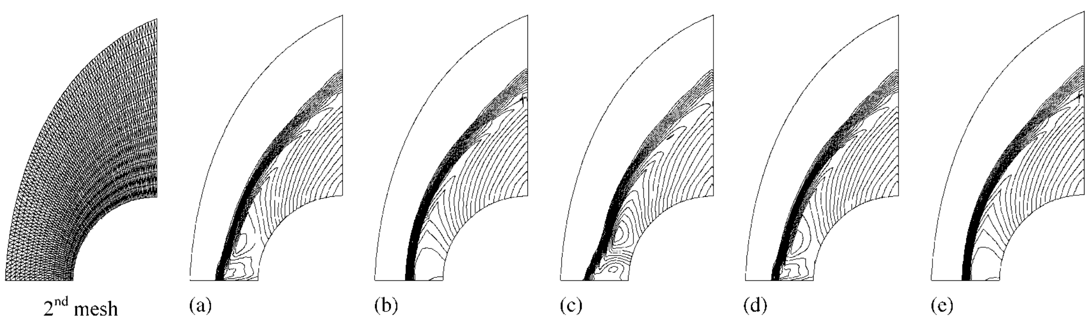


Figure 3. Density contours of a Mach 15 flow over a blunt body (second mesh): (a) $\mathscr{Roe}$; (b) $\mathscr{RoePA}$; (c) $\mathscr{RoeSA}$; (d) $\mathscr{RoeVL}$; and (e) $\mathscr{RoeVLPA}$.

elements in the circumferential direction; the $\mathscr{RoePA}$ and $\mathscr{RoeVLPA}$ provide a realistic flow behavior while the others exhibit a small bump on the bow shock as shown in Figure 3(a)–(e). The carbuncle phenomenon can be clearly seen in a very elongated mesh normal to the shock as shown in Figure 4(a)–(e). Similar to the previous two meshes, the $\mathscr{RoePA}$ and $\mathscr{RoeVLPA}$ still provide reasonable flow solutions with a small glitch on the shock by the $\mathscr{RoePA}$, while the carbuncle phenomena can be observed in the results of the $\mathscr{Roe}$, $\mathscr{RoeSA}$, and $\mathscr{RoeVL}$.

These numerical experiments have shown that the carbuncle phenomenon is influenced by a mesh alignment problem and very sensitive to the mesh aspect ratio as reported in Reference [6]. The very elongated meshes normal to the shock promote such numerical instabilities.

### 2.3. *Quirk's test (odd–even decoupling)*

The second test case is a Mach 6 moving shock along odd–even grid perturbation in a straight duct [2]. The computational domain consists of a uniform triangular mesh with 800 and 20 equal intervals along the axial and transverse directions of the duct, respectively. The inflow is given as a strong shock entering the duct on the left boundary. The outflow is imposed at the outlet on the right boundary. The upper and lower boundaries are considered as slip walls. The grids along the duct centerline are perturbed in the transverse direction with a magnitude of $\pm 10^{-6}$. Figure 5(a)–(e) shows the density contours of the normal shock at three locations along the duct.



DOI: 10.1002/fld

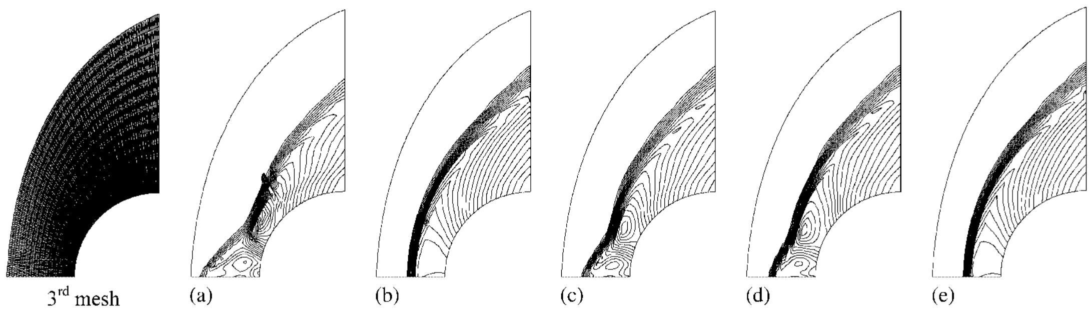


Figure 4. Density contours of a Mach 15 flow over a blunt body (third mesh): (a) $\mathscr{Roe}$; (b) $\mathscr{RoePA}$; (c) $\mathscr{RoeSA}$; (d) $\mathscr{RoeVL}$; and (e) $\mathscr{RoeVLPA}$.

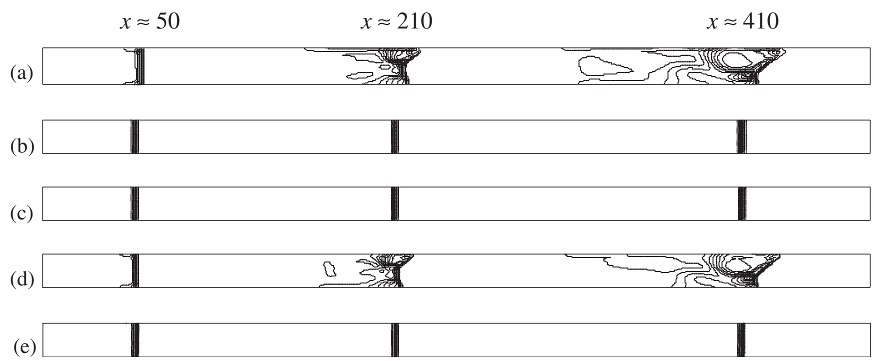


Figure 5. Density contours of a Mach 6 moving shock along odd–even grid perturbation: (a) $\mathscr{Roe}$; (b) $\mathscr{RoePA}$; (c) $\mathscr{RoeSA}$; (d) $\mathscr{RoeVL}$; and (e) $\mathscr{RoeVLPA}$.

The $\mathscr{RoePA}$, $\mathscr{RoeSA}$, and $\mathscr{RoeVLPA}$ can provide accurate shock resolutions, whereas the $\mathscr{Roe}$ and $\mathscr{RoeVL}$ suffer from numerical instabilities. The capture of exact contact discontinuity and strict stability cannot be simultaneously satisfied in any upwind scheme [10]. The experiments suggest that additional dissipation injection to the vorticity and entropy waves is thus needed to stabilize Roe's scheme as done by the $\mathscr{RoePA}$, $\mathscr{RoeSA}$, and $\mathscr{RoeVLPA}$.

### *2.4. The kinked Mach stem*

The problem statement consists of a strong planar shock at Mach 5 moving from the left to right boundaries and reflecting on a ramp to cause the double-Mach reflection (DMR) configuration. The inflow is given by a strong planar shock entering the domain along the left boundary, the 46° ramp is considered as a slip wall, and the outflow conditions are imposed along the other boundaries. Figure 6(a)–(e) shows the density contours of a DMR simulation obtained from different schemes at time $t = 0.1$. The $\mathscr{RoePA}$, $\mathscr{RoeSA}$ and $\mathscr{RoeVLPA}$ provide reasonably accurate solutions such that the kinked Mach stem is recovered with a slightly broken-down incident shock. The $\mathscr{Roe}$ and $\mathscr{RoeVL}$, however, yield the broken-down incident shock with the severely kinked Mach stem



DOI: 10.1002/fld

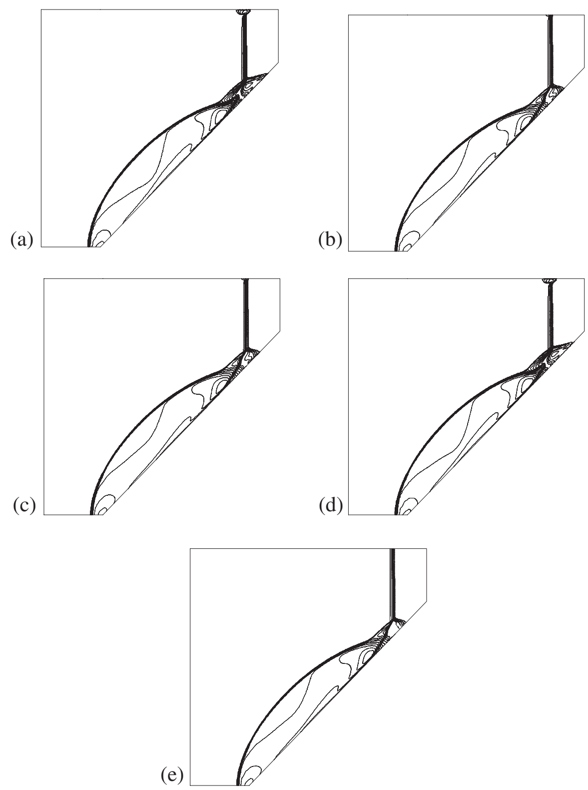

Figure 6. Density contours of a kinked Mach stem from a Mach 5 shock moving over a 46° ramp: (a) $\mathscr{Roe}$; (b) $\mathscr{RoePA}$; (c) $\mathscr{RoeSA}$; (d) $\mathscr{RoeVL}$; and (e) $\mathscr{RoeVLPA}$.

giving rise to a spurious triple point. The mechanism behind this failure is not fully understood. The numerical experiments suggest that such a solution may be caused by the insufficient dissipation that cannot counteract the transverse perturbation [2, 10]. Adding more dissipation to the vorticity and entropy waves may be an appropriate way to control the kinking and the broken-down incident shock.

### 2.5. *The expansion shock*

The original Roe's scheme may produce a nonphysical expansion shock because it does not satisfy the entropy condition. To illustrate this phenomenon, a high-speed flow over a forward-facing step [11] is investigated. The problem statement is given by a uniform flow at Mach 3 entering the domain from the left boundary, the outflow conditions are prescribed on the right boundary, and the upper and lower boundaries are considered as the slip walls. The computed density contours at time $t = 10.5$ are shown in Figure 7(a)–(e). The figures show that the $\mathscr{Roe}$ and $\mathscr{RoePA}$ produce nonphysical expansion shocks on top of the step corner, whereas the $\mathscr{RoeSA}$, $\mathscr{RoeVL}$, and $\mathscr{RoeVLPA}$ provide realistic solutions. These expansion shocks can be eliminated by fixing the acoustic waves by using either $\mathscr{RoeVL}$ or $\mathscr{RoeSA}$.



DOI: 10.1002/fld

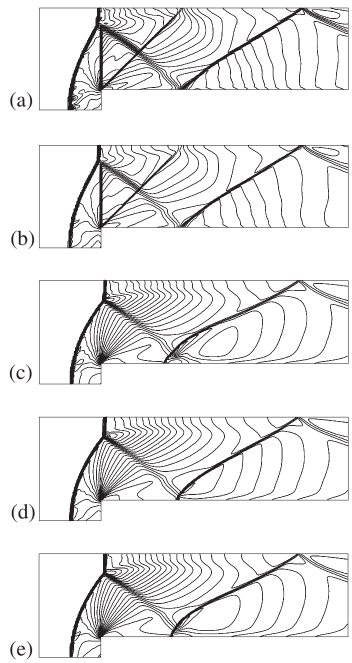

Figure 7. Density contours of a Mach 3 flow over a forward-facing step: (a) $\mathscr{Roe}$; (b) $\mathscr{RoePA}$; (c) $\mathscr{RoeSA}$; (d) $\mathscr{RoeVL}$; and (e) $\mathscr{RoeVLPA}$.

The numerical experiments on the above four examples also suggest that the healing of instability for Roe's flux-difference splitting scheme on a structured triangular mesh are as follows:

(a) The numerical instability that causes undershoot of the computed quantities, such as the internal energy, density, or pressure, resulting in a negative speed of sound, can be healed by adding appropriate dissipation to the acoustic waves ($k=1$ and 4).
(b) For healing the carbuncle phenomenon or spurious numerical oscillation, appropriate dissipation should be added to the entropy and vorticity waves (for $k=2$ and 3).

To illustrate the sawtooth instability mechanism of the above-described methods, the odd–even decoupling problem is solved on a two-dimensional uniform mesh. The discrete solution at $t^n$, for $j$ being even and odd numbers, is given by [2]

$$\rho_j^n = \rho \pm \hat{\rho}^n, \quad p_j^n = p \pm \hat{p}^n, \quad u_j^n = u, \quad v_j^n = 0 \tag{8}$$

where the plus and minus signs indicate the odd and even values of $j$, respectively. $\hat{\rho}^n$ and $\hat{p}^n$ are the amplitudes of sawtooth profiles of the density and the pressure, respectively. The eigenvalues and the amplitudes of the sawtooth profiles at $t^{n+1}$ are given by

$\mathscr{Roe}$:

$$\lambda_{1,4} = \tilde{a} \quad \text{and} \quad \lambda_{2,3} = 0 \tag{9a}$$

$$\hat{\rho}^{n+1} = \hat{\rho}^n - \frac{2v_y}{\tilde{a}^2}\hat{p}^n \tag{9b}$$

$$\hat{p}^{n+1} = \hat{p}^n(1-2v_y) \tag{9c}$$



DOI: 10.1002/fld

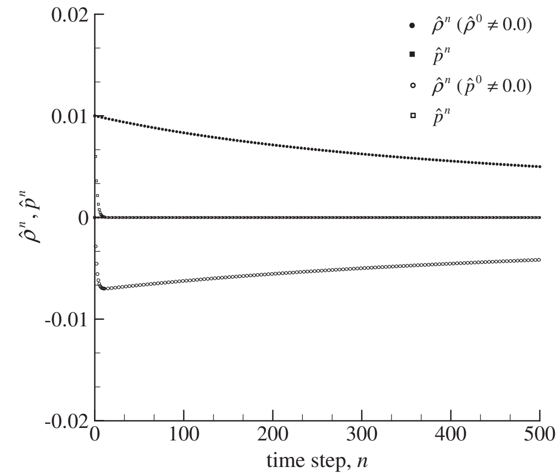


Figure 8. Odd–even decoupling problem: effect of $\kappa = 1$ to density and pressure perturbations on the *RoeVLPA*.

*RoePA*, *RoeSA* and *RoeVLPA*:

$$\lambda_{1,4} = \tilde{a} \quad \text{and} \quad \lambda_{2,3} = \eta^{\mathrm{PA}} \tag{10a}$$

$$\hat{\rho}^{n+1} = \hat{\rho}^n \left(1 - \frac{2v_y \eta^{\mathrm{PA}}}{\tilde{a}}\right) - \frac{2v_y}{\tilde{a}^2}\left(1 - \frac{\eta^{\mathrm{PA}}}{\tilde{a}}\right)\hat{p}^n \tag{10b}$$

$$\hat{p}^{n+1} = \hat{p}^n (1 - 2v_y) \tag{10c}$$

where $v_y = \tilde{a}\Delta t/\Delta y$.

Equations (9b)–(9c) indicate that *Roe* damps the pressure perturbation under the CFL condition but promotes the density perturbation and causes numerical instability as shown in Figure 5(a). For *RoeSA*, *RoePA*, and *RoeVLPA*, the coupling of the pressure perturbation into the density perturbation in Equations (10b)–(10c) is damped by $\eta^{\mathrm{PA}}$. This prevents *RoeSA*, *RoePA* and *RoeVLPA* from yielding flaw solutions as in the *Roe*. It is noted that *RoeVL* provides the same results as *Roe* since $\eta^{\mathrm{VL}}$ is always zero by this analysis. For the case of *RoeVLPA*, with the initial disturbances of the density and pressure fields being $\hat{\rho}^0$ and $\hat{p}^0$, respectively, the density perturbation after $n$ time steps is given as follows:

$$\hat{\rho}^n = \left(1 - \frac{2v_y \eta^{\mathrm{PA}}}{\tilde{a}}\right)\left(\hat{\rho}^0 - \frac{\hat{p}^0}{\tilde{a}^2}\right) \tag{11}$$

As $n \to \infty$ and $\eta^{\mathrm{PA}}$ is adjusted until $2v_y\eta^{\mathrm{PA}}/\tilde{a}$ is equal to 1, the density perturbation is then damped to 0. This is the reason for the constant $\kappa$ inclusion in Equation (7) in order to sustain the numerical stability.

To examine the effect of the value $\kappa$ to the density and pressure perturbations, the procedure described in Section 5 of Reference [6] is employed by considering the uniform flow of $(\rho_0, u_0, v_0, p_0) = (1.0, \neq 0.0, 0.0, 1.0)$ over the domain of the odd–even decoupling problem. The



DOI: 10.1002/fld

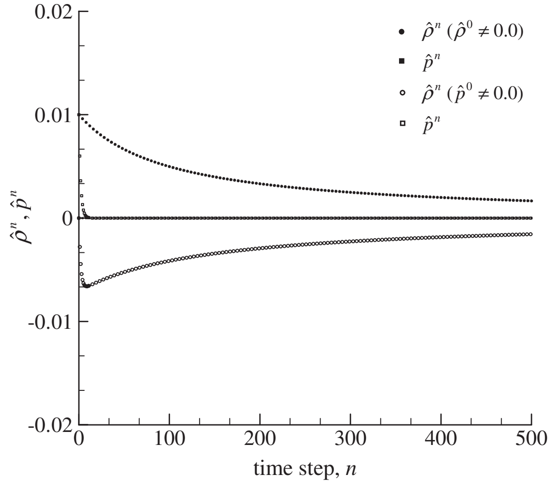


Figure 9. Odd–even decoupling problem: effect of $\kappa = 5$ to density and pressure perturbations on the $\mathcal{RoeVLPA}$.

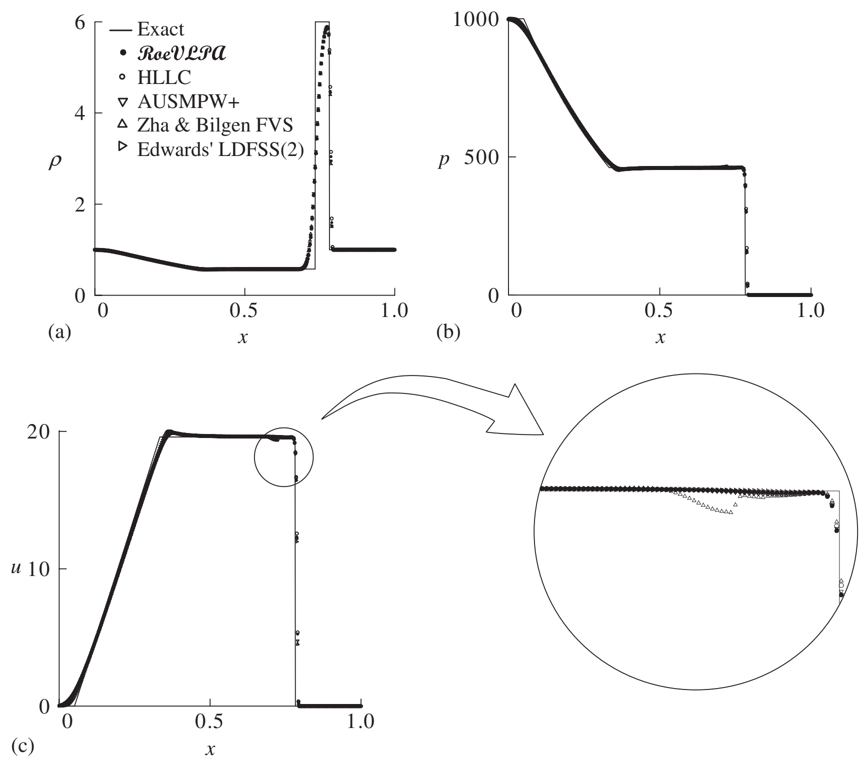


Figure 10. Comparative exact and first-order numerical solutions at time $t = 0.012$ for the strong shock problem: (a) density; (b) pressure; and (c) $u$-velocity.



DOI: 10.1002/fld

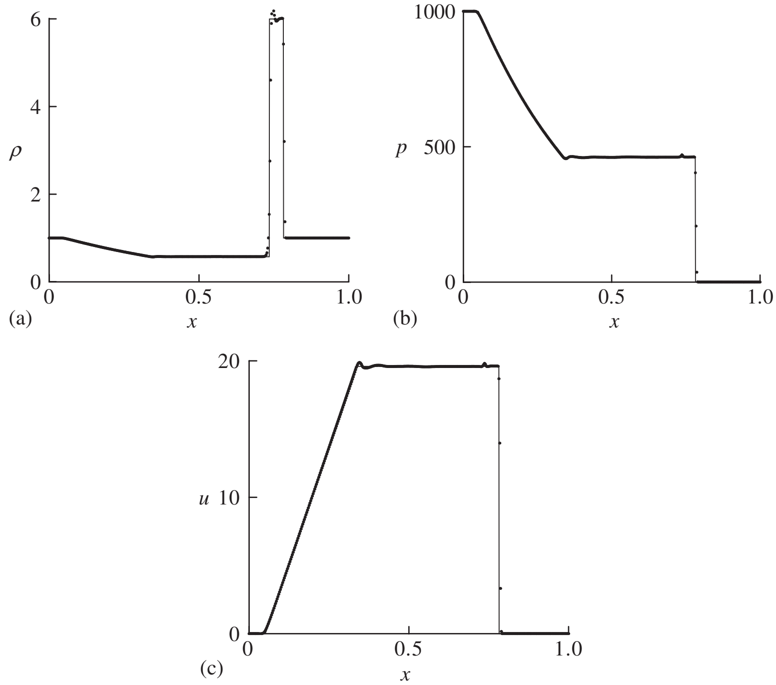


Figure 11. Comparative exact and higher-order numerical solutions ($\mathscr{RoeVLPA}$) at time $t=0.012$ for the strong shock problem: (a) density; (b) pressure; and (c) $u$-velocity.

initial perturbations along the $y$-direction are given by $(\hat{\rho}_0, \hat{u}_0, 0.0, \hat{p}_0)$, and the initial flow conditions are $(\rho^0, u^0, v^0, p^0) = (1.0 \pm \hat{\rho}_0, u_0 \pm \hat{u}_0, 0.0, 1.0 \pm \hat{p}_0)$. Figures 8 and 9 show the response of the density and pressure perturbations by using the value of $\kappa$ as 1.0 and 5.0, respectively. The density and pressure perturbations are damped in time with a higher rate on a larger value of $\kappa$. The damping rate is relatively small as compared with the carbuncle-free FVS scheme described in Reference [6]. However, numerical experiments have confirmed that a small dissipation value to prevent $\lambda_2$ and $\lambda_3$ from becoming zero is enough to stabilize Roe's scheme. It should also be noted that the value of $\kappa$ as 1 is adequate for healing of numerical instability for the first-order accuracy scheme. In the latter case, the $\mathscr{RoeVLPA}$ provides identical solutions as those obtained from the $\mathscr{RoePA}$.

## 3. HIGHER-ORDER EXTENSION AND EVALUATION

Solution accuracy from the first-order formulation described in the preceding section can be improved by using a higher-order formulation for both space and time. A higher-order spatial discretization is achieved by applying the Taylor series expansion to the cell-centroids so that the flow quantities on the face are given by

$$\mathbf{q}_{\text{face}} = \mathbf{q}_{\text{centroid}} + \psi \nabla \mathbf{q} \cdot \mathbf{r} \tag{12}$$



DOI: 10.1002/fld

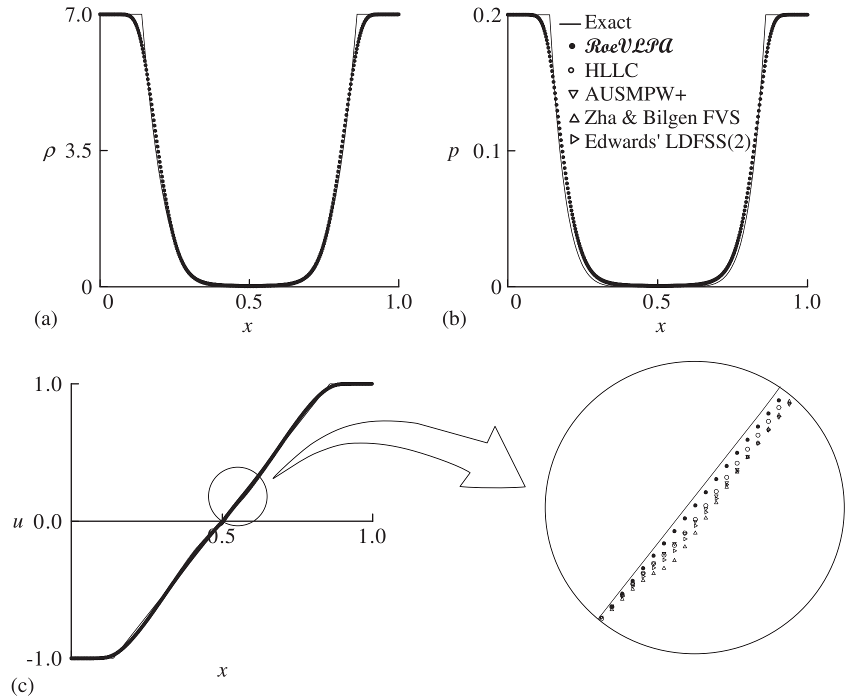


Figure 12. Comparative exact and first-order numerical solutions at time $t=0.3$ for the symmetric rarefaction wave problem: (a) density; (b) pressure; and (c) $u$-velocity.

where $\mathbf{q}=[\rho\ u\ v\ p]^{\mathrm{T}}$ consists of the primitive variables of the density, the velocity components, and the pressure, respectively; $\nabla\mathbf{q}$ represents the gradient of the variables; and $\mathbf{r}$ is the vector projected to the given element's face. The value $\psi$ in Equation (12) represents the limiter for preventing spurious oscillations that may occur in the region of high solution gradients. In this study, Venkatakrishnan's limiter function [12] is selected. In the determination of the gradient, $\nabla\mathbf{q}$, the least-square procedure [13] is employed to yield exact gradients for linear functions on an arbitrary mesh [14]. The second-order accurate Runge–Kutta time stepping method [15] is implemented for transient solutions. To reduce computational effort, the local element time steps are used for the steady-state analysis, while the minimum global time step based on spectral radii [16] is used for the transient analysis.

The higher-order extension of the proposed $\mathscr{RoeVLPA}$ method described in the preceding section is evaluated by solving several test cases on a structured triangular mesh. The selected test cases are (1) the strong shock problem, (2) symmetric rarefaction wave problem, and (3) Mach 2 shock reflection over a wedge. For all test cases the $L_2$ norm of density residual is used to measure the convergence of the flow solutions.

### *3.1. The strong shock problem*

The one-dimensional strong shock problem [17] is simulated on a $1.0\times 0.1$ domain, which is discretized by uniform triangular elements ($400\times 40$). The initial conditions are given by



DOI: 10.1002/fld

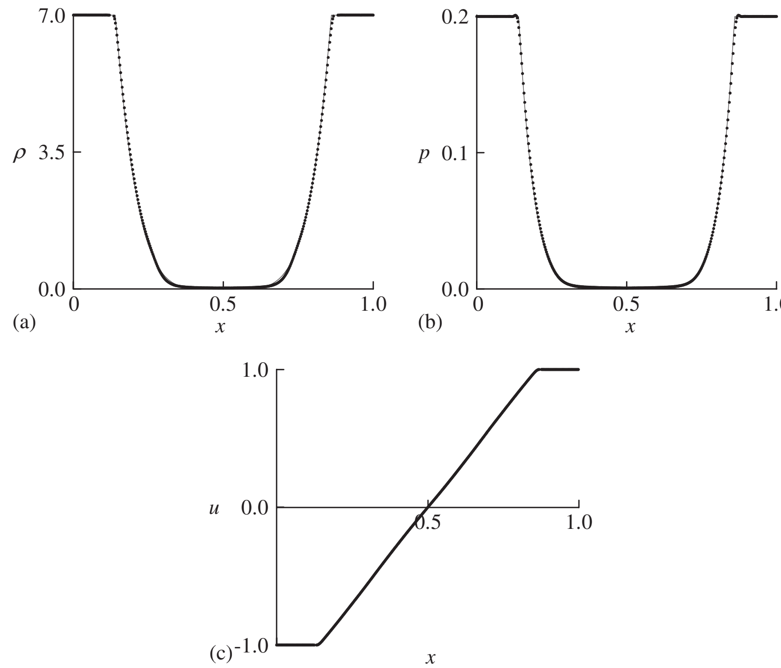


Figure 13. Comparative exact and higher-order numerical solutions ($\mathscr{R}\mathit{oe}\mathscr{VLPA}$) at time $t=0.3$ for the symmetric rarefaction wave problem: (a) density; (b) pressure; and (c) $u$-velocity.

$(\rho,u,p)_L=(1.0,0.0,1000.0)$ and $(\rho,u,p)_R=(1.0,0.0,0.01)$. Because of the very strong shock wave, the validity of the ideal gas equation of state may be questioned, but the purpose of using this test case is for numerical experiment to evaluate the different schemes. Another reason for choosing this problem is that the shock and the contact discontinuity are very close to each other, within only about nine elements. It is thus very difficult for most of the numerical schemes to capture both the shock and the contact discontinuities within such few elements. Figure 10 shows the first-order results at time $t=0.012$ obtained from the five schemes, $\mathscr{R}\mathit{oe}\mathscr{VLPA}$, HLLC [18], AUSM-PW+ [19], Zha and Bilgen FVS [20], and Edwards' LDFSS(2) [21]. The density computed from these schemes are very similar but very diffusive compared with the exact solution. The Zha and Bilgen FVS scheme has a slight oscillation near the contact discontinuity as shown by the pressure and the $u$-velocity plots. The constant value $\kappa$ in Equation (7) used for this problem is 0.85 and 1.75, for the first-order and the higher-order scheme, respectively. Figure 11 shows that the higher-order solutions are improved but are still yielding oscillations slightly near the expansion fan and the contact discontinuity.

### 3.2. *Symmetric rarefaction wave problem*

The initial conditions of the symmetric rarefaction wave problem [16] are given by $(\rho,u,p)_L=(7.0,-1.0,0.2)$ and $(\rho,u,p)_R=(7.0,1.0,0.2)$ such that they produce vacuum at the center of the domain. Figure 12 shows the first-order results at time $t=0.3$. The density and pressure distributions obtained from five schemes agree well with the exact solutions. The $\mathscr{R}\mathit{oe}\mathscr{VLPA}$ and HLLC schemes give better $u$-velocity than the others because both schemes preserve the contact



DOI: 10.1002/fld

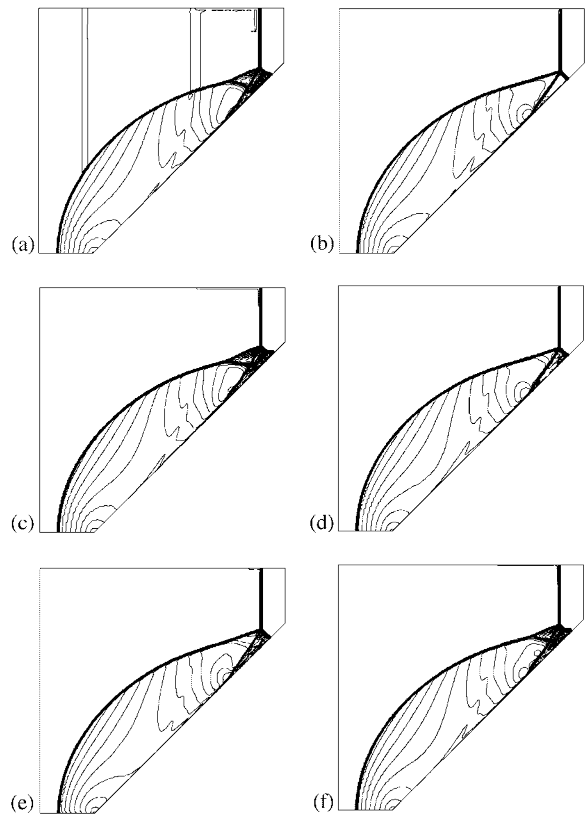


Figure 14. Comparison of density contours of a Mach 2 shock reflection over a wedge: (a) $\mathscr{R}oe\mathscr{V}\mathscr{L}\mathscr{P}\mathscr{A}$ with $\kappa = 1$; (b) $\mathscr{R}oe\mathscr{V}\mathscr{L}\mathscr{P}\mathscr{A}$ with $\kappa = 6$; (c) HLLC; (d) AUSM-PW+; (e) Zha and Bilgen FVS; and (f) Edwards' LDFSS(2).

discontinuity. Figure 13 shows the higher-order solutions of the $\mathscr{R}oe\mathscr{V}\mathscr{L}\mathscr{P}\mathscr{A}$ that compare well with the exact solutions.

### *3.3. Mach 2 shock reflection over a wedge*

A Mach 2 shock reflection over a wedge at 46° [22] is used to evaluate the performance of the proposed $\mathscr{R}oe\mathscr{V}\mathscr{L}\mathscr{P}\mathscr{A}$ as compared with the other schemes for a more complex flow problem. All numerical experiments were performed using a structured triangular mesh with a spacing of 0.0039 for a total of 91 471 cells. Figure 14 compares the density contours obtained from the five schemes with higher-order solution accuracy at time $t = 0.35$, where the shock wave approximately locates at a distance of 0.1 from the right boundary. Using the constant $\kappa = 1$ in the $\mathscr{R}oe\mathscr{V}\mathscr{L}\mathscr{P}\mathscr{A}$ scheme, the incident shock is slightly broken-down with a severely kinked Mach stem due to an inappropriate numerical dissipation added to the vorticity and entropy waves as shown in Figure 14(a). The solution from the $\mathscr{R}oe\mathscr{V}\mathscr{L}\mathscr{P}\mathscr{A}$ is improved with good shock and Mach stem resolution after using $\kappa = 6$ as shown in Figure 14(b). Figure 14(c) and (f) shows the solutions from the HLLC and LDFSS(2) schemes that also exhibit kinked Mach stem and a spurious triple point. Figure 14(d) and (e) shows the more dissipative solutions from the AUSM-PW+ and Zha



DOI: 10.1002/fld

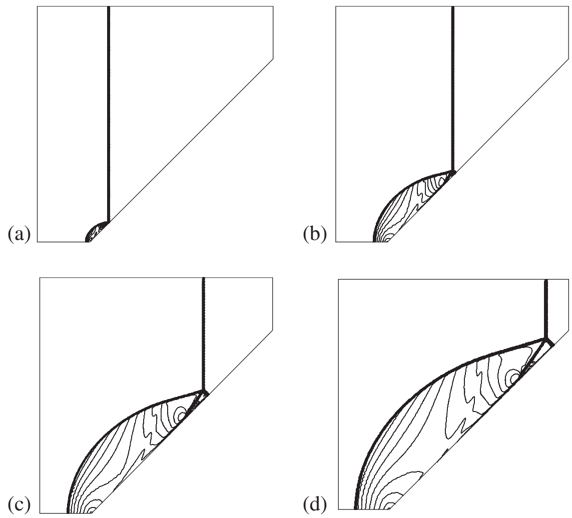


Figure 15. Density contours of a Mach 2 shock reflection over a wedge at four time steps ($\mathscr{RoeVLPA}$ with $\kappa = 6$): (a) $t = 0.05$; (b) $t = 0.15$; (c) $t = 0.25$; and (d) $t = 0.35$.

Table I. Comparison of CPU time usage for a Mach 2 shock reflection over a wedge.

| Scheme | CPU time/cell/iteration (μs) |
|---|---|
| $\mathscr{Roe}$ | 7.01 |
| $\mathscr{RoeVLPA}$ | 14.13 |
| HLLC | 7.10 |
| AUSM-PW+ | 10.09 |
| Zha–Bilgen FVS | 6.79 |
| Edwards' LDFSS(2) | 7.13 |

and Bilgen FVS schemes that yield good flow resolution with little spurious triple point and a slightly kinked Mach stem near the wall. The transient solutions at the four different times obtained from $\mathscr{RoeVLPA}$ are presented in Figure 15(a)–(d). The computations were performed using a laptop computer with AMD Turion 64M processor, 1 GB RAM, and running on Windows XP professional. The CPU times (time/cell/iteration) used by the six schemes are shown in Table I. The $\mathscr{RoeVLPA}$ uses more CPU time than the other schemes, with approximately twice as required by the original $\mathscr{Roe}$ scheme. More CPU time is needed by the additional procedure used in the mixed multidimensional entropy fix scheme as shown in Equation (7).

## 4. CONCLUSIONS

A mixed entropy fix method was proposed to improve the numerical stability of Roe's flux-difference splitting scheme. The proposed method was evaluated by several well-known test cases and found to heal nonphysical solutions that may arise from the use of the original Roe's scheme. To further improve solution accuracy, the higher-order spatial and second-order Runge–Kutta temporal discretizations were also implemented. The method was found to provide accurate solutions for both steady-state and transient flow test cases as compared with other well-known schemes.

## ACKNOWLEDGEMENTS

The authors are pleased to acknowledge the Thailand Research Fund (TRF) for supporting this research paper.

## REFERENCES

1. Perry KM, Imlay ST. Blunt-body flow simulations. *Twenty-fourth AIAA/SAE/ASME/ASEE Joint Propulsion Conference*, *AIAA Paper-88-2904*, Boston, MA, 1988.
2. Quirk JJ. A contribution to the great Riemann solver debate. *International Journal for Numerical Methods in Fluids* 1994; **18**:555–574.
3. Harten A. High resolution schemes for hyperbolic conservation laws. *Journal of Computational Physics* 1983; **49**:357–393.
4. Van Leer B, Lee WT, Powell KG. Sonic-point capturing. *AIAA 9th Computational Fluid Dynamics Conference*, *AIAA Paper-89-1945-CP*, Buffalo, New York, 1989.
5. Sanders R, Morano E, Druguet MC. Multidimensional dissipation for upwind schemes: stability and applications to gas dynamics. *Journal of Computational Physics* 1998; **145**:511–537.
6. Pandolfi M, D'Ambrosio D. Numerical instabilities in upwind methods: analysis and cures for the 'Carbuncle' phenomenon. *Journal of Computational Physics* 2001; **166**:271–301.
7. Roe PL. Approximate Riemann solvers, parameter vectors, and difference schemes. *Journal of Computational Physics* 1981; **43**:357–372.
8. Dechaumphai P, Phongthanapanich S. High-speed compressible flow solutions by adaptive cell-centered upwinding algorithm with modified *H*-correction entropy fix. *Advances in Engineering Software* 2003; **34**:533–538.
9. Druguet MC, Zeitoun DE. Influence of numerical and viscous dissipation on shock wave reflections in supersonic steady flows. *Computers and Fluids* 2003; **32**:515–533.
10. Gressier J, Moschetta JM. Robustness versus accuracy in shock-wave computations. *International Journal for Numerical Methods in Fluids* 2000; **33**:313–332.
11. Woodward P, Colella P. The numerical simulation of two-dimensional fluid flow with strong shocks. *Journal of Computational Physics* 1984; **54**:115–173.
12. Venkatakrishnan V. Convergence to steady state solutions of the Euler equations on unstructured grids with limiters. *Journal of Computational Physics* 1995; **118**:120–130.
13. Anderson WK, Bonhaus DL. An implicit upwind algorithm for computing turbulent flows on unstructured grids. *Computers and Fluids* 1994; **23**:1–21.
14. Haselbacher A, Blazek J. Accurate and efficient discretization of Navier–Stokes equations on mixed grids. *AIAA Journal* 2000; **38**:2094–2102.
15. Shu CW, Osher S. Efficient implementation of essentially non-oscillatory shock-capturing schemes. *Journal of Computational Physics* 1988; **77**:439–471.
16. Linde T, Roe PL. Robust Euler codes. *Thirteenth Computational Fluid Dynamics Conference*, *AIAA Paper-97-2098*, Snowmass Village, CO, 1997.
17. Toro EF. *Riemann Solvers and Numerical Methods for Fluid Dynamics*. Springer: Berlin, 1999.
18. Toro EF, Spruce M, Speares W. Restoration of the contact surface in the HLL-Riemann solver. *Shock Waves* 1994; **4**:25–34.
19. Kim KH, Kim C, Rho OH. Methods for the accurate computations of hypersonic flows: I.AUSMPW+ scheme. *Journal of Computational Physics* 2001; **174**:38–80.

20. Zha GC. Comparative study of upwind scheme performance for entropy condition and discontinuities. *AIAA Paper-99-3348*, 1999.
21. Edwards JR. A low-diffusion flux-splitting scheme for Navier–Stokes calculations. *Computers and Fluids* 1997; **26**:635–659.
22. Takayama K, Jiang Z. Shock wave reflection over wedges: a benchmark test for CFD and experiments. *Shock Waves* 1997; **7**:191–203.




DOI: 10.1002/fld